Aerodynamic interaction effects of tip-mounted propellers installed on the horizontal tailplane

Van Arnhem, Nando; Sinnige, Tomas; Stokkermans, Tom C.A.; Eitelberg, Georg; Veldhuis, Leo L.M.

DOI
10.2514/6.2018-2052

Publication date
2018

Document Version
Final published version

Published in
AIAA Aerospace Sciences Meeting

AIAA SciTech Forum
8–12 January 2018, Kissimmee, Florida
2018 AIAA Aerospace Sciences Meeting

10.2514/6.2018-2052

Aerodynamic Interaction Effects of Tip-Mounted Propellers Installed on the Horizontal Tailplane

Nando van Arnhem*, Tomas Sinnige†, Tom C. A. Stokkermans†, Georg Eitelberg‡ and Leo L. M. Veldhuis‡
Delft University of Technology, Delft, 2629 HS, The Netherlands

This paper addresses the effects of propeller installation on the aerodynamic performance of a tailplane featuring tip-mounted propellers. A model of a low aspect ratio tailplane equipped with an elevator and a tip-mounted propeller was installed in a low-speed wind-tunnel. Measurements were taken with an external balance and surface pressure taps to determine the aerodynamic characteristics of the tailplane, while the flowfield in the wake of the model was investigated using particle-image velocimetry. The experimental data are supported by CFD analyses, involving both transient simulations of the full-blade configuration and steady-state simulations the propeller replaced by an actuator-disk model. The upstream effects on the propeller time-average and time-accurate thrust and normal-forces are found to be limited for different tailplane operating conditions. It is shown that for a given propeller rotation direction, the load distribution on the tailplane is highly dependent on the direction of elevator deflection. The rotation direction of the tailplane tip-vortex relative to the propeller swirl therefore significantly affects the integral loads on the tailplane, resulting in differences in the normal-force gradient and elevator effectiveness.

Nomenclature

b	=	Tailplane span [m]
c	=	Tailplane chord [m]
c_d	=	Section drag coefficient, $\frac{d}{q_\infty c}$
C_N	=	Tailplane normal-force coefficient, $\frac{N}{q_\infty b c}$
C_{N_α}	=	Gradient of normal-force versus angle of attack curve $[\frac{1}{\text{rad}}]$
C_{N_p}	=	Propeller normal-force coefficient $\frac{N_p}{\rho_\infty \Omega^2 D^4}$
$C_{N_{\delta_\text{e}}}$	=	Change in C_N by elevator deflection, $\frac{\text{d}C_N}{\text{d}\delta_\text{e}}$ $[\frac{1}{\text{rad}}]$
C_p	=	Pressure coefficient, $\frac{p-p_\infty}{q_\infty}$
C_T	=	Propeller thrust coefficient, $\frac{T}{\rho_\infty \Omega^2 D^4}$
c_n	=	Section normal-force coefficient, $\frac{n}{q_\infty c}$
c_n'	=	Fluctuations of section normal-force coefficient
D	=	Propeller diameter [m]
d	=	Section drag $[\frac{\text{N}}{\text{m}}]$
J	=	Propeller advance ratio, $\frac{V_\infty}{\Omega D}$
N	=	Tailplane normal-force [N]
N_p	=	Propeller normal-force [N]
n	=	Section normal-force $[\frac{\text{N}}{\text{m}}]$
p	=	Pressure [Pa]
p_∞	=	Atmospheric pressure [Pa]
q_∞	=	Freestream dynamic pressure, $\frac{1}{2}\rho_\infty V_\infty^2$ [Pa]
R	=	Propeller radius [m]
r	=	Propeller radial coordinate [m]
S_ref	=	Reference area [m^2]
T	=	Propeller thrust [N]
t	=	Tailplane thickness [m]
V_∞	=	Freestream velocity $[\frac{\text{m}}{\text{s}}]$
x'	=	Coordinate along airfoil chordline [m]
x, y, z	=	Cartesian coordinates [m]
α	=	Angle of attack [deg]
Γ_b	=	Bound circulation $[\frac{\text{m}^2}{\text{s}}]$
δ_e	=	Elevator deflection [deg]
η	=	Spanwise coordinate, $\frac{2z}{b}$
θ	=	Propeller phase angle [deg]
ρ_∞	=	Density of freestream $[\frac{\text{kg}}{\text{m}^3}]$
ϕ	=	Swirl angle in propeller rotation axis system [deg]
Ω	=	Propeller rotational speed $[\frac{1}{\text{s}}]$
ω	=	Vorticity $[\frac{1}{\text{s}}]$

*Ph.D. Candidate, Flight Performance and Propulsion Section, Faculty of Aerospace Engineering, N.vanArnhem@tudelft.nl; AIAA member.
†Ph.D. Candidate, Flight Performance and Propulsion Section, Faculty of Aerospace Engineering; AIAA member.
‡Full Professor, Flight Performance and Propulsion Section, Faculty of Aerospace Engineering; AIAA member.

I. Introduction

Driven by the desire for high subsonic flight, the major focus of aircraft engine development is on turbofan engines. However, the constant pursuit of higher propulsive efficiency redirected propulsion studies to the inherently more efficient turboprop propulsion system [1–3]. As a result, there is a renewed interest in open-rotor integration, ranging from wingtip-mounted distributed propulsion (e.g. the proposed NASA X-57 Maxwell concept [4]), tail-mounted open-rotors [5, 6], to tail-mounted single-rotating propellers. Tail-mounted propeller configurations are of interest primarily because of their potential to reduce the cabin noise compared to wing-mounted propellers [2]. Several studies [2, 7] have considered the feasibility of a number of tail-mounted propeller configurations, such as T-tail configurations with pylon-mounted propellers and integrated configurations with propellers mounted on the tip of the horizontal tailplane, as illustrated in Fig. 1.

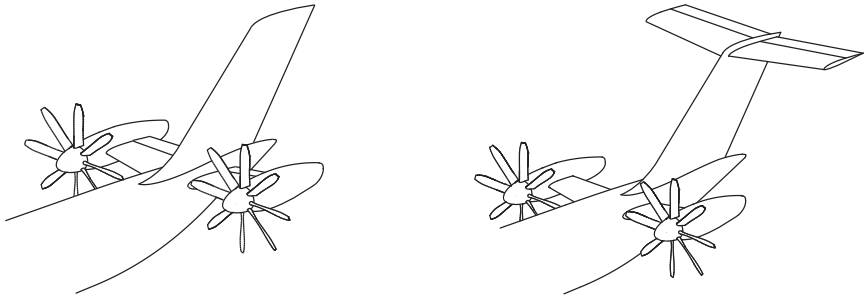

(a) Horizontal-tailplane mounted (b) Pylon mounted

Fig. 1 Examples of tail-mounted propeller configurations.

In order to successfully exploit the benefits of the tailplane-mounted propeller configuration, technical challenges need to be resolved in the fields of aerodynamics, flight dynamics, and structural integration [2, 8]. The analysis of a tractor propeller in close proximity with an aerodynamic surface has primarily been conducted for the wing-mounted propeller configuration, e.g. in Ref. [9]. Existing studies on tip-mounted propellers (e.g Refs [10–13]) have mainly focused on the efficiency benefits for wingtip-mounted propeller configurations. Typical aerodynamic quantities which are relevant for the propeller–tailplane combination are the change in normal-force due to elevator deflection, the normal-force gradient, the maximum down force, and the side forces on the propeller, tailplane, and nacelle.

In this paper, the focus is on the typical aerodynamic interaction phenomena between the propeller and tailplane which are present for a tailplane-mounted arrangement. In Fig. 2a, a schematic is shown of the typical interaction effects occurring for such a configuration. The propeller slipstream has a downstream effect on the tailplane loading distribution compared to propeller-off conditions.

The tailplane also induces an upstream effect by altering the inflow at the propeller disk due to in-plane and out-of-plane induced velocities. The out-of-plane induced velocity is a combination of the tailplane blockage and the velocity induced by the tailplane bound vortex. The in-plane velocities are primarily induced by the tailplane's trailing vortex system and its bound vortex. Compared to wing-mounted propeller installation, there are a number of significant differences in the type and magnitude of aerodynamic interaction. Tailplane-mounted propellers interact with an aerodynamic surface which has a low aspect ratio and the propeller is relatively large compared to the tailplane span. The result is that the propeller affects a lift distribution which strongly varies in spanwise direction, leading to a complex interaction of the tailplane tip-vortex and the propeller-induced flowfield. In addition, during nominal operation the tailplane is required to produce a normal-force in both positive and negative directions. Therefore, the magnitude of the propeller–tailplane interactions is also influenced by the elevator which changes the tailplane loading, as depicted in Fig. 2b.

In general, the propellers mounted on the tips of a wing are counter-rotating because it increases the efficiency of the propeller–wing combination [10]. As commercial propeller aircraft are generally equipped with co-rotating propellers for economical reasons [2], it can be expected that this will also be the case for future tailplane-mounted propeller aircraft. Therefore, this asymmetry in the loading distribution on the tailplane should be addressed.

In this paper, a combined experimental–numerical analysis is presented of a tractor propeller mounted on a symmetric, low-aspect-ratio tailplane equipped with an elevator. It can be recognized that the setup is also valuable for

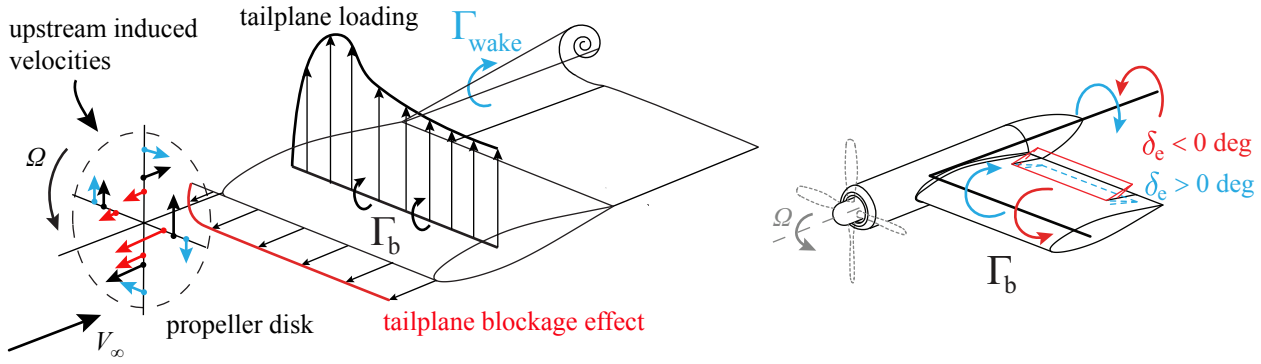

(a) Schematic of propeller–tailplane interaction.

(b) Effect of elevator deflection on the direction of the tailplane bound vortex

Fig. 2 Schematic of the propeller-tailplane interaction in (a) and the effect of an elevator deflection on the direction of bound circulation of the tailplane in (b).

the analysis of wingtip-mounted propellers. Two levels of CFD simulations were performed: full-blade (FB) simulations and actuator-disk (AD) simulations. The purpose of these simulations is twofold: They support the experimentally assessed cases and allow for the analysis of the co-rotating propeller configuration.

II. Experimental Setup

A. Wind-Tunnel Facility & Models

The experimental campaign was performed at the Low-Turbulence Tunnel (LTT) at Delft University of Technology. This low-speed, closed-return wind tunnel features a test section with cross-section of 1.80 × 1.25 m. At the selected freestream velocity of 40 m/s, the turbulence level is below 0.1%. The model was suspended from a ground plane installed in the top part of the test section, which acted as a symmetry plane. This reduced the effective height of the test section to 1.00 m.

A semi-installed propeller–tailplane configuration was simulated by connecting a tractor-propeller model to the tip of a symmetric tailplane model, as shown in Fig. 3. The propeller was a scaled model of a de Havilland Canada Beaver propeller. It featured a diameter of 0.237 m and its four blades were set to a blade pitch angle of 23.9 deg at 75% of the radius. The radial distributions of the blade chord and twist angle are provided in Ref. [14]. The propeller was driven by a 5.5 kW three-phase induction motor housed inside a nacelle with a diameter of 0.070 m.

The nacelle was connected to a straight, symmetric tailplane model with a chord length of 0.240 m, a span of 0.292 m, and a NACA 64_2A015 profile. The model featured a 25%-chord plain flap, which was used to represent an elevator. Transition was forced using a 2.5 mm wide trip wire made out of silicon carbide particles, positioned at 12% of the chord from the leading edge of the tailplane model. Chordwise rows of static-pressure ports were available at 8 spanwise locations, as discussed in Section II.B.2. The streamwise propeller–tailplane spacing was fixed to 43% of the propeller diameter. The tailplane model was connected to a rotating disk integrated into the ground plane, allowing for measurements at nonzero angle of incidence. Photographs of the propeller–tailplane model installed in the LTT are depicted in Fig. 4.

It may be recognized that the propeller–tailplane model is a conceptual representation of the configurations shown in Fig. 1. For example, the selected propeller has a relatively low number of blades and the fraction of the elevator washed by the propeller slipstream is relatively small. The choice for the tailplane and propeller was based on available hardware and on the benefit that other studies [9, 14, 15] have used the same models.

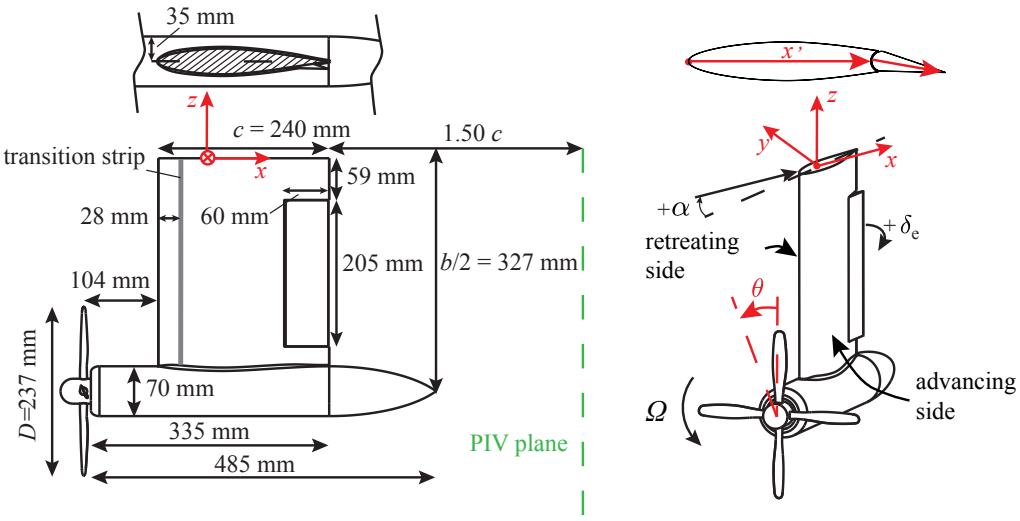

Fig. 3 Technical drawing of the tip-mounted propeller–tailplane model including the location of the PIV survey plane.

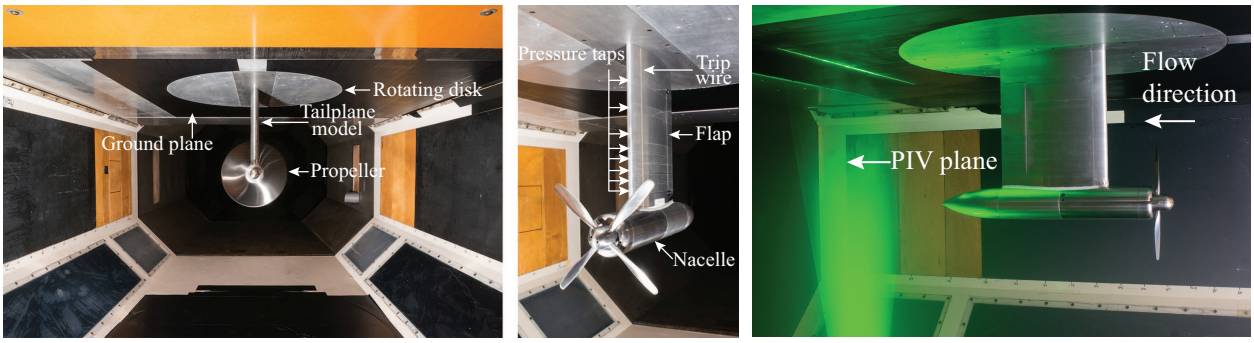

Fig. 4 Tip-mounted propeller setup installed in the Low-Turbulence Tunnel at Delft University of Technology.

B. Measurement Techniques

1. External-Balance Measurements

The integral forces and moments generated by the propeller–tailplane combination were acquired using an external six-component balance. Measurements were taken both with and without the propeller blades installed to allow for an assessment of the aerodynamic interaction effects caused by the propeller slipstream.

2. Surface-Pressure Measurements

The tailplane model contained 408 pressure taps, providing local measurements of the pressure distribution at 8 spanwise locations: $\eta = -[0.19, 0.34, 0.49, 0.55, 0.61, 0.68, 0.74, 0.80]$. Since at each chordwise position the pressure ports were cross-connected in spanwise direction, the measurements were taken per pressure row, with all other rows closed by tape. The pressures from each spanwise row were simultaneously recorded at a sampling rate of 5 Hz using an electronic pressure scanner and averaged over a measurement time of 3 seconds to obtain the final results per datapoint.

3. Velocity-Field Measurements Using Particle-Image Velocimetry

Flowfield measurements were taken in the wake of the model using stereoscopic particle-image velocimetry (PIV). Three measurements planes were used, oriented perpendicularly to the flow at $1.5c$ from the trailing edge of the tailplane model. Table 1 provides an overview of the data-acquisition and postprocessing characteristics of the PIV setup. The cameras were traversed simultaneously in the vertical direction to allow for measurements in three different planes, together covering the entire wake of the propeller–tailplane model. The results from the three measurement planes

were combined in postprocessing to obtain a final field of view with dimensions of 360 × 485 mm. Figures 3 and 4 illustrate the axial position of the field of view with respect to the model. Both phase-uncorrelated and phase-locked measurements were taken, with phase-locking achieved using a one-per-revolution-trigger signal integrated into the motor driving the propeller. Six blade phase angles were considered with a 15 deg spacing between consecutive angles. The velocity data obtained from the PIV evaluations were complemented by pressure measurements using a wake rake, consisting of 50 total-pressure probes and 12 static-pressure probes. These data are not discussed in this paper.

Table 1 Data-acquisition and postprocessing characteristics of the stereoscopic PIV setup.

Parameter	Value	Parameter	Value
PIV setup	Stereoscopic	Pulse separation	40 μs
Laser	200 mJ Nd:YAG	Max. particle displacement	25 pixel
Cameras	2× 16 Mpixel CCD	Image pairs	300^a, 1000^b
Objective	200 mm $f/4$	Interrogation window size	24 × 24 pixel
Field-of-view (FOV) size	360 × 485 mm	Window overlap factor	50%
FOV position ($\Delta X_{\mathrm{TE}}/c$)	1.5	Vector spacing	0.9 mm

^{a} phase-locked measurements, ^{b} phase-uncorrelated measurements

C. Test Cases

All measurements were taken at a freestream velocity of 40 m/s. This freestream velocity was selected based on a tradeoff between Reynolds number and available motor power allowing for sustained testing with the available hardware. The propeller was operated at four different thrust settings ranging from approximately $C_T = 0.02$ to 0.12 [14], corresponding to advance ratios J of 1.0, 0.9, 0.8, and 0.7. Moreover, measurements were taken with a dummy spinner installed to obtain a baseline to which the propeller-on measurements could be compared. Three elevator settings were evaluated: $\delta_e = [0, +10, -10]$ deg. The positive and negative elevator deflection settings were considered to compare the cases for which the rotation direction of the tailplane tip-vortex was opposite or equal to that of the propeller swirl. The case with zero elevator deflection served as baseline and represents a pylon-mounted tractor-propeller configuration. The aerodynamic performance measurements using the external balance and surface-pressure taps were taken at angles of attack α ranging from -20 deg up to $+20$ deg. The PIV measurements of the flowfield in the wake of the setup were only taken at an angle of attack of $\alpha = 0$ deg.

III. Computational Setup

The numerical analysis of the propeller–tailplane model was performed by solving the RANS equations for compressible flow at two levels of fidelity. Time-accurate full-blade propeller simulations were performed to capture the unsteady nature of the propeller–tailplane interaction. This time-dependent interaction study was supported by the application of an actuator-disk model to simulate the co-rotating case, for which no experimental data were available. An overview of the computational strategy is given below. For an extensive description the reader is referred to Ref. [15], which also includes a detailed grid-convergence study and a validation of the numerical results with the experimental data.

Simulations were performed for the intermediate thrust setting at $J = 0.8$, and angles of attack of 0 deg and $+10$ deg. For the case without angle of attack, two elevator settings were simulated ($\delta_e = [-10, +10]$ deg), while for the case at $\alpha = +10$ deg only the elevator setting of -10 deg was evaluated.

The propeller-tailplane model was simulated in a domain representing the wind-tunnel test section, as shown in Fig. 5. Therefore, the results can be compared to the experimental results which were not corrected for wind-tunnel wall effects. The propeller blades, spinner, nacelle, tailplane, and elevator were modeled as no slip walls, while the front part of the nacelle in the rotating domain was modeled by a moving wall. All wind-tunnel walls were modeled as slip walls, except the top wall on which a no-slip condition was enforced to capture the development of the boundary layer on the tunnel ceiling and its interaction with the tailplane. For the propeller-off cases, the propeller domain was replaced by a domain with only a spinner, or a domain suitable for an actuator-disk model. Also isolated propeller simulations were performed, which included the propeller, spinner, and nacelle geometry.

ANSYS® Fluent Release 16.0 [16], an unstructured finite volume cell-centered solver, was used to perform the

simulations. The flow was prescribed to be fully turbulent using the Spalart–Allmaras turbulence model with the strain/vorticity-based production equation. An average y^+ of 1 was obtained, resulting in a resolved boundary layer. The full-blade simulations were solved in a time-accurate manner, with a time step equivalent to 2 deg propeller rotation with 35 inner iterations. The simulations performed with the actuator-disk model were solved in a steady-state manner, resulting in a significant reduction of the computational cost. The actuator-disk model is based on the addition of momentum and energy source terms to the RANS equations, similar to Ref. [17], and is extensively discussed in Ref. [15].

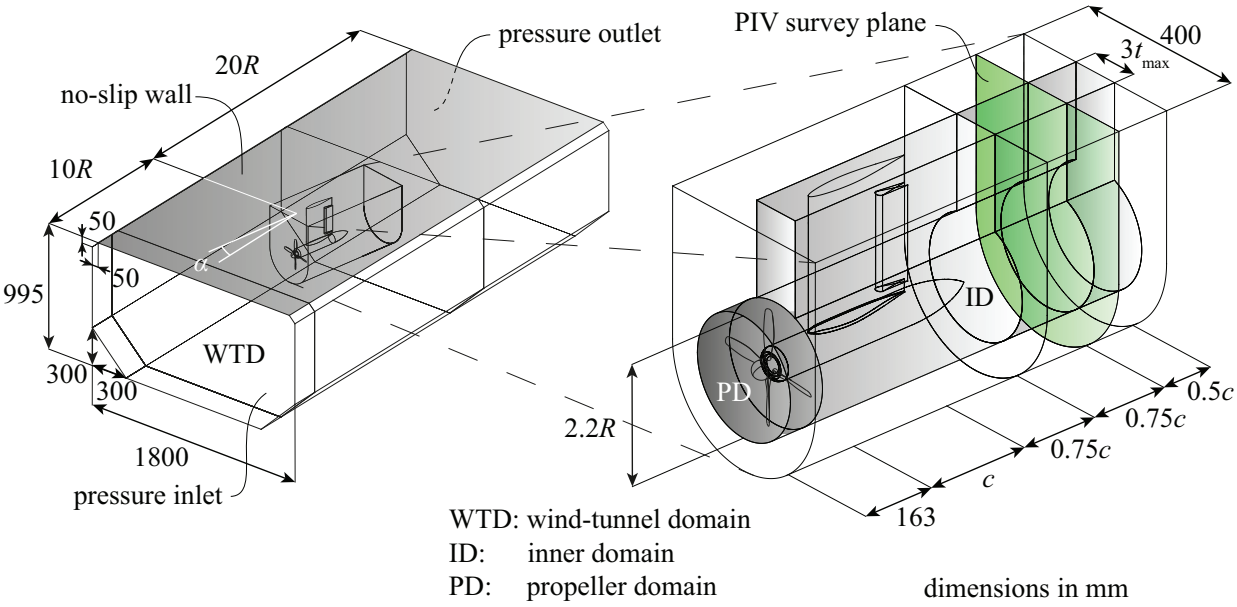

Fig. 5 Computational domain and boundary conditions used for the simulations.

IV. Results

In the following sections the experimental and numerical results on the propeller–tailplane aerodynamic interactions are presented. First, the flowfield downstream of the propeller–tailplane combination is assessed in Section IV.A. The upstream effect on the propeller loading is then addressed in Section IV.B. Subsequently, the loading distributions on the tailplane are presented in Section IV.C, while the intergral loads on the propeller–tailplane are discussed in Section IV.D. Finally, section IV.E evaluates the case with two tip-mounted propellers which are co-rotating.

A. Interaction Between Propeller Slipstream and Tailplane Tip-Vortex

The swirl of the flow behind the propeller–tailplane model provides an indication of the loading on the tailplane and the in-plane induced losses of the system. The flowfield measured using PIV can therefore provide insight into the interaction between the propeller and the tailplane [10]. Figure 6 depicts the distribution of the swirl angle in the PIV plane for a medium-thrust condition at an advance ratio $J = 0.8$ and a 0 deg angle of attack. It can be seen that the interaction with the tailplane leads to a deformation of the slipstream, characterized by a shear of the part of the slipstream which directly impinged on the tailplane. This deformation was visualized before in Ref. [14] for the case of a pylon-mounted propeller, while similar effects occur for the conventional wing-mounted configuration [9, 18]. The deformation is the result of the variation in circulation along the tailplane (Fig. 2a), inducing a crossflow along the tailplane span which is opposite in direction on the pressure and suction sides respectively. Another cause of the slipstream deformation is the initial deformation of the slipstream in the leading edge region of the tailplane due to vortex bending, which is further addressed in Section IV.C.

Figure 6 also shows that the $\delta_e = 0$ deg case features a positive swirl in the order of 5 deg in the outer region of the slipstream and a negative swirl in the order of -5 deg at the inner region of the slipstream. The swirl in the outer region is dominated by the propeller-induced swirl, while the swirl in the inner region is dominated by the tailplane-induced tip-vortex. The presence of the negative swirl angle in the inner region of the slipstream indicates that there is a finite loading on the tailplane which induces a swirl opposite to the propeller swirl. The relative swirl induced by the propeller

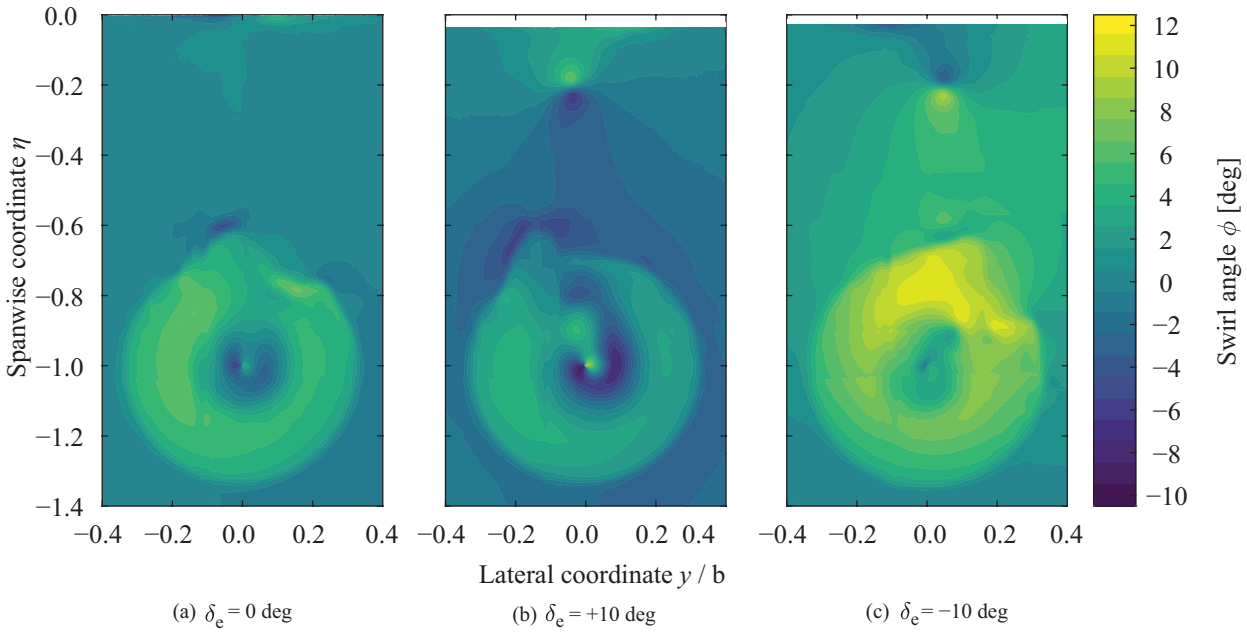

Fig. 6 Time-averaged swirl angle in a plane 1.5c downstream the trailing edge of the tailplane, obtained with PIV at $J = 0.8, C_T = 0.09$ and $\alpha = 0$ deg.

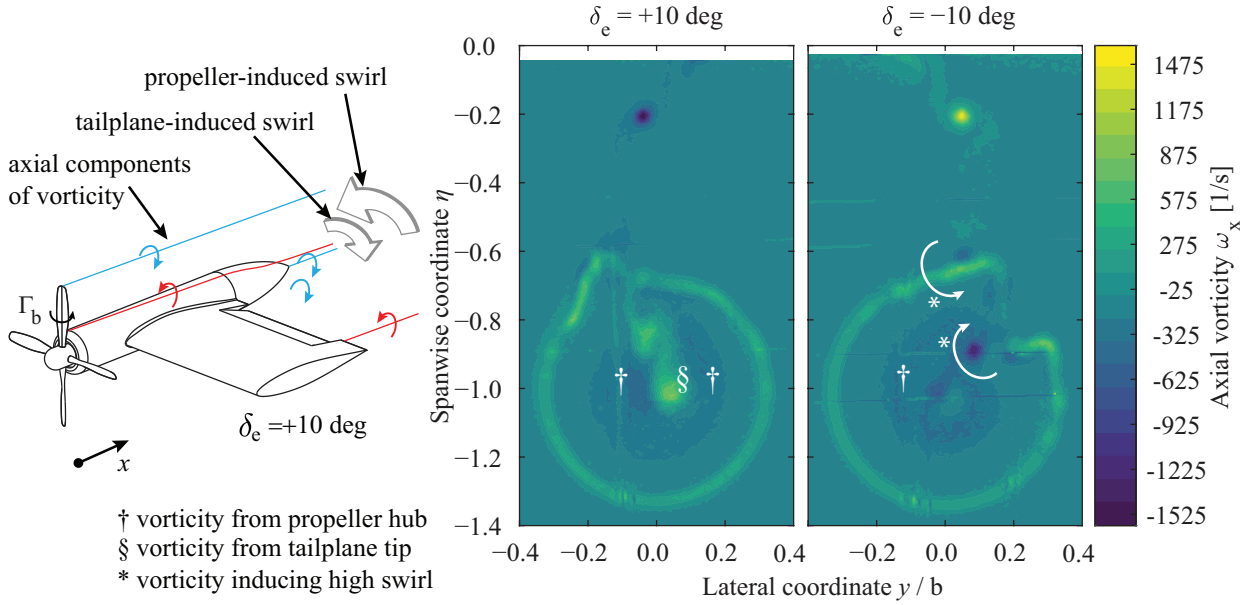

Fig. 7 Schematic of axial vorticity of the propeller and tailplane, and the phase-averaged axial component of vorticity obtained in the PIV plane.

and tailplane change when the elevator is deflected. The case of $\delta_e = +10$ deg (Fig. 6b) shows a reduction in swirl angle compared to the case without elevator deflection. The lift on the tailplane is increased by the positive elevator deflection, leading to an increase in strength of the tailplane tip-vortex. Since this vortex induces a swirl in the opposite direction of the propeller slipstream, the average swirl angle in the slipstream decreases compared to the case without elevator deflection. The opposite is the case at $\delta_e = -10$ deg (Fig. 6c), for which the elevator deflection results in a tailplane tip-vortex rotating in the same direction as the propeller-induced swirl, thus enhancing the swirl downstream of the tailplane.

The modification of the swirl downstream of the propeller–tailplane model caused by the different elevator deflections can be understood by considering the combined vortex systems of the propeller and tailplane, as sketched in Fig. 7. In this figure the propeller bound vortex and the axial component of vorticity of the propeller slipstream and tailplane are sketched. The magnitude and the direction of these vortices induce the in-plane velocities v and w. To illustrate the distribution of axial vorticity ω_x in the slipstream, contours of the axial vorticity are also shown in Fig. 7. The flowfield consists of both positive and negative ω_x in the inner region of the slipstream. The positive ω_x is shed by the tip of the tailplane and the outboard edge of the elevator, while the negative ω_x is the sum of the propeller hub vortices. For the negative elevator deflection, all axial vorticity in the inner region is in the same direction, explaining the higher average swirl angle shown in Fig. 6c. Figure 6c also shows that the region of the slipstream which has been sheared in the $\delta_e = -10$ deg case, is characterized by a particularly high swirl angle. It is thought that this swirl was induced by the combination of the elevator outboard tip-vortex and the axial vorticity from the propeller tip vortices, as indicated by the two semicircular arrows in Fig. 7. The contours show that the propeller tip vortices which impinged on the tailplane exhibit an increase in ω_x, mainly due to the bending of the tip-vortex around the leading edge of the tailplane, as discussed in Section IV.C. Because the elevator tip-vortex is not centered in the slipstream, the region spanned by these two counter-rotating vortices experiences a particularly high swirl velocity.

B. Upstream Interaction: Installation Effects on Propeller Forces

The presence of the tailplane causes a nonuniform inflow to the propeller, resulting in a nonuniform blade loading which affects the propeller thrust, torque, and in-plane forces. The latter are especially relevant for tip-mounted tailplane configurations, for which the moment arm from propeller to the aircraft's center of gravity is relatively large. As a result, the impact of the in-plane propeller forces on the aircraft's trim and stability characteristics is typically larger than for conventional wing-mounted propeller configurations.

The upstream effect of the tailplane on the propeller loading was investigated using the time-accurate CFD data. Figure 8a shows the thrust distribution along the propeller radius for the isolated and the installed configurations at an angle of attack of 0 deg. The associated numerical values are given in Table 2, which includes the time-averaged values of thrust coefficient and normal-force coefficient together with the maximum positive and negative excursions of the time-accurate distributions from their mean. In Fig. 8a the time-averaged loading is displayed by the lines, with the surrounding shaded area indicating the loading fluctuations in time. For the isolated propeller, the blade loading is nearly constant, except in the hub region ($r/R < 0.4$) where separation occurred due to the nearly circular propeller sections in this region (see [14]). For the installed configuration, this flow separation at the root remained unchanged, while the loading on the outboard part of the blade was increased due to the nonuniform inflow caused by the tailplane. As indicated in Table 2, the time-averaged C_T value is increased by approximately 3% for the case with an elevator deflection of +10 deg. The increase in the time-averaged thrust is directly related to the combination of a locally different axial velocity and angle of attack compared to freestream conditions, both induced by the tailplane.

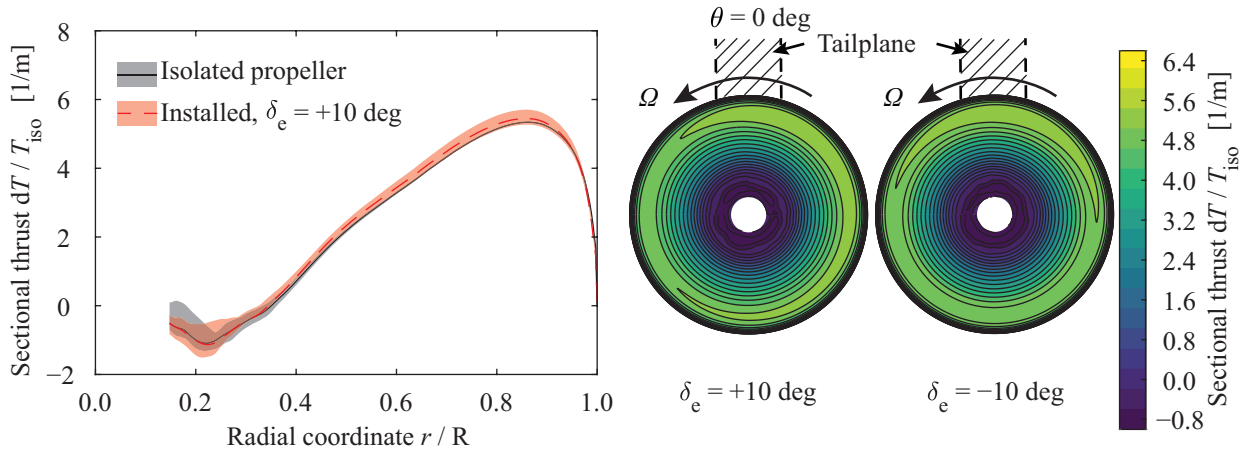

(a) Radial thrust distribution of one propeller blade, installed versus isolated

(b) Effect of elevator deflection on azimuthal thrust distribution

Fig. 8 Effect of tailplane installation on the computed propeller loading at α = 0 deg.

Table 2 Effect of tailplane installation on the propeller thrust and normal-force: computed time-averaged values and maximum fluctuations.

		Isolated	Installed, $\delta_e = +10$ deg	Installed, $\delta_e = -10$ deg
$C_T \cdot 100$	$\alpha = 0$ deg	$9.08^{+0.33}_{-0.41}$	$9.37^{+0.19}_{-0.23}$	$9.31^{+0.22}_{-0.14}$
	$\alpha = +10$ deg	$9.63^{+0.18}_{-0.15}$	N/A	$9.92^{+0.18}_{-0.15}$
$C_{N_p} \cdot 100$	$\alpha = 0$ deg	0	$-0.04^{+0.05}_{-0.08}$	$-0.11^{+0.05}_{-0.05}$
	$\alpha = +10$ deg	$0.76^{+0.09}_{-0.07}$	N/A	$0.79^{+0.09}_{-0.10}$

Apart from the effect on the time-averaged thrust, the nonuniformity of the propeller inflow leads to variations in the thrust on the local blade sections of approximately ±2% of the time-averaged values. To visualize the azimuthal distribution of the unsteady propeller loading caused by the tailplane, Fig. 8b displays contours of the thrust distribution for the cases with elevator deflections of +10 and −10 deg. It can be seen that both positive and negative elevator deflections result in a higher thrust contribution in the region where the propeller blades are in the vicinity of the tailplane's leading edge. In this region, the upstream effect is characterized by the tailplane blockage and the net upwash induced by the tailplane bound vortex and the trailing vortex system. For the case with a $\delta_e = +10$ deg the upwash is in the same direction as the propeller rotation direction, decreasing the local angle of attack of the blade sections. The opposite situation occurs for a negative elevator deflection. Since for both elevator deflections the thrust is increased in this region, it is thought that the thrust increase is primarily the result of the locally reduced axial velocity due to blockage by the tailplane, which causes a decreased effective advance ratio for the blade sections.

Apart from the modification of the blade loading in front of the tailplane, a difference can be observed in the blade loading on the two sides of the tailplane (i.e. around $\theta = 90$ deg and $\theta = 270$ deg). It is thought that the loading in these regions is primarily affected by the tailplane bound vortex, as sketched in Fig. 2a. On the pressure side of the tailplane, there is locally a reduction of inflow velocity to the propeller, while on the tailplane suction side there is locally an increase in inflow. For the case with $\delta_e = +10$ deg, the $\theta = 270$ deg side of the propeller disk corresponds to the pressure side of the tailplane, hence the propeller loading is increased in this region. This effect is most pronounced for the case with an elevator deflection of +10 deg, since for this setting the tailplane loading was highest. For an elevator deflection of −10 deg, on the other hand, the same mechanism was practically absent, because the tailplane loading was smaller. As a result, the impact of tailplane installation on the time-averaged thrust coefficient was smaller for the case with $\delta_e = -10$ deg than for $\delta_e = +10$ deg, which is confirmed by Table 2.

The propeller normal-force in the installed condition with an elevator deflection of +10 deg amounts to 0.4% of the installed thrust, while for the negative elevator deflection the normal-force is 1.2% of the installed thrust. If the analogy is made with a propeller under incidence [19], the upwash induced by the tailplane would result in a propeller normal-force with its sign depending on the direction of the tailplane bound vortex. However, for both elevator deflections the propeller normal-force is negative. The increased thrust around $\theta = 0$ deg which is present for both elevator deflections, is associated with an increase in torque (not shown in this paper). This higher torque results in a net in-plane force in y direction, resulting in a negative propeller normal force.

At nonzero angle of attack, the propeller loading and hence the propeller slipstream become more nonuniform in the azimuthal direction. Figure 9a shows the mean and the fluctuations of the thrust distribution on one propeller blade for the isolated and installed configurations at an angle of attack of +10 deg. For the isolated propeller, significant loading fluctuations now occur throughout the revolution. This is as expected considering the cyclic change in angle of attack experienced by the blade sections while rotating through the asymmetric inflow field [9]. The installation of the tailplane with an elevator deflection of −10 deg has a minor impact on the loading distribution, which is apparently dominated by the angle-of-attack effect. Compared to the isolated propeller, the time-averaged thrust again increased by 3%. However, this was mostly due to decreased drag in the root region of the blade, where flow separation occurred as discussed before. As a result, this difference can also be the result of the finite averaging-time used to compute the time-averaged data from the time-accurate simulations [15]. On the outboard part of the blade, where the flow remained attached, the differences in time-averaged loading were negligible between the isolated and installed configurations. As opposed to the small impact on the time-averaged blade loading, the increased nonuniformity of the inflow in the installed configuration directly translated into larger loading fluctuations.

The azimuthal distribution of sectional thrust is presented in Fig. 9b. For the isolated configuration, a typical azimuthal distribution of thrust is shown for a propeller under incidence (e.g. in [20]). By installation of the propeller on the tailplane, it can be observed that the location of maximum thrust shifts toward the pressure side of the tailplane.

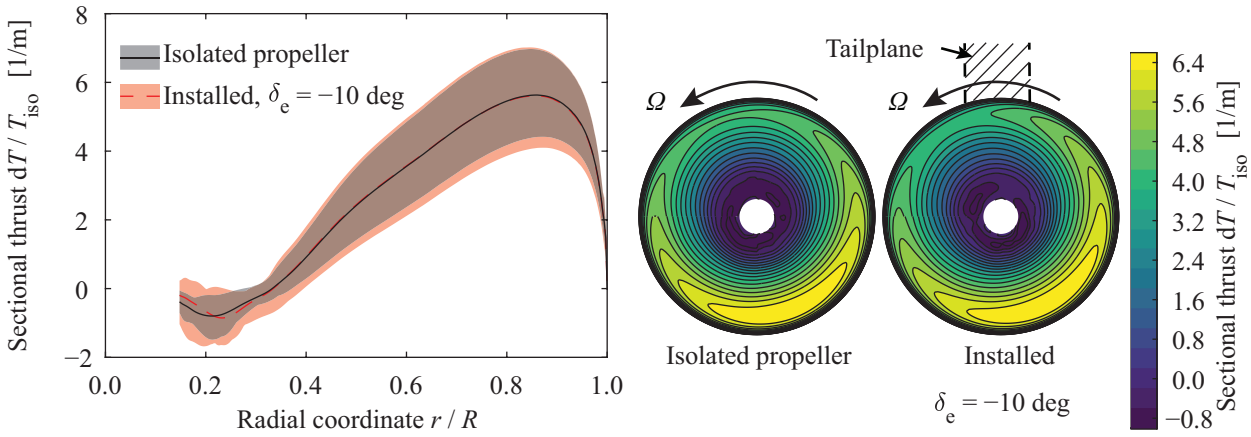

(a) Radial thrust distribution of one propeller blade, installed versus isolated.

(b) Installed versus isolated, azimuthal thrust distribution

Fig. 9 Effect of tailplane installation on the computed propeller loading at α = +10 deg.

This is thought to be the result of the out-of-plane velocities induced by the tailplane bound vortex, as sketched in Fig. 2a. The thrust around $\theta = 0$ deg is slightly reduced compared to the isolated case, which may indicate that the effect of the tailplane-induced upwash is larger than its blockage effect on the propeller loading.

Table 2 shows that the normal-force of the installed propeller is similar to the normal-force of the isolated propeller. Although the tailplane installation results in a different propeller loading distribution compared to isolated conditions, the changes in blade forces are such that the net in-plane force of the propeller is not significantly altered.

C. Downstream Interaction: Loading Distributions on Tailplane

With the propeller present, the inflow to the tailplane is modified due to the locally increased dynamic pressure and swirl in the slipstream. As a result of this downstream interaction, the tailplane loading distribution is modified. The impact of propeller thrust setting and elevator setting on the change in tailplane loading was analyzed using both experimental and numerical data. Figure 10 depicts the measured spanwise distributions of the normal-force coefficient for the three elevator deflections and a range of advance ratios. The normal-force was computed by integrating the experimentally obtained pressure distributions. Two angles of attack are considered: $\alpha = 0$ deg (Fig. 10a) and $\alpha = +10$ deg (Fig. 10b). The propeller installation increases the normal-force on the tailplane by locally inducing a larger angle of attack and a higher dynamic pressure, with the largest increase in c_n observed in the part of the tailplane immersed in the propeller slipstream. The loading distribution on the part of the tailplane outside of the slipstream is also altered due to the changed trailing vorticity compared to propeller-off conditions, as was also discussed in Ref. [9]. The $\alpha = 0$ deg case (Fig. 10a) shows that a positive deflection of the elevator results in a significantly larger change of the normal-force compared to a negative deflection. Increasing the angle of attack to 10 deg, the difference between positive and negative elevator deflections reduces. At this angle of attack, the net normal-force on the tailplane is positive. Therefore, the tailplane tip-vortex was contra-rotating with the propeller for both the positive and negative flap settings. Consequently, the change in aerodynamic interaction between the two flap settings was now only related to a difference in tip-vortex strength, thereby reducing the offset between the two elevator settings compared to the result obtained at $\alpha = 0$ deg. The limited spatial resolution of the experimental data in the spanwise direction masks the gradients in the loading distribution near the slipstream edge and the flap edges. Therefore, the CFD data were assessed to obtain more detailed loading distributions for the case at $J = 0.8$. Figure 11 presents the resulting spanwise distributions of the time-averaged normal-force coefficient for the positive and negative flap settings. For comparison reasons, both the propeller-off and propeller-on configurations are considered, while the available experimental data are also included.

The time-averaged numerical and experimental data show a good agreement in terms of distribution, although an offset is observed, with the CFD data generally predicting a higher normal-force than measured in the experiment. It should be noted that the finite number of chordwise pressure taps introduces an inaccuracy in the pressure integration of the measured results, specifically in the elevator region. Additionally, it was found that the tailplane had a small misalignment with the freestream flow, which may explain the small differences in the measured normal-force between $\delta_e = +10$ deg and $\delta_e = -10$ deg. The presence of the elevator is reflected in the loading distributions by the rapid

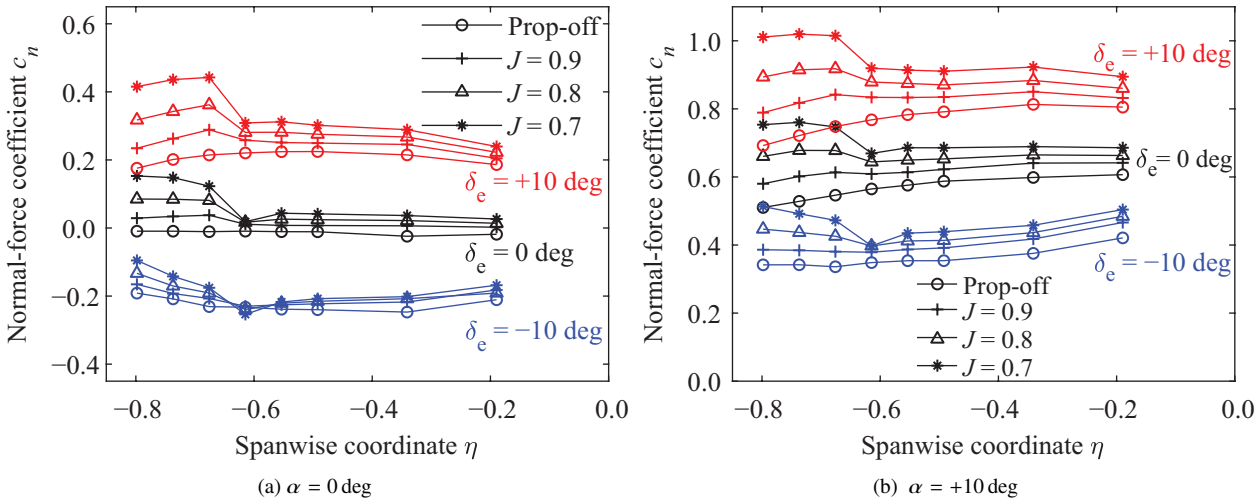

Fig. 10 Spanwise distributions of normal-force coefficient obtained by integration of the measured pressure distributions.

changes in c_n along the span at $\eta = -0.18$ and -0.81. The local decrease of c_n at the spanwise location where the propeller tip is located, is likely the result of the locally decreased static and total pressure at the edge of the propeller slipstream introduced by the propeller tip vortices, observed before in e.g. Ref. [18]. The fluctuations in normal-force obtained from the CFD analysis highlight that variations in c_n occur primarily in the propeller slipstream region, with a magnitude of $c_n' = \pm 0.01$. The magnitude of these fluctuations was comparable for the cases at $\delta_e = +10$ deg and $\delta_e = -10$ deg. Variations on the mean c_n outside the slipstream may be considered negligible. These changes are an effect of the time-dependent vortex field associated with the tailplane sections immersed in the propeller slipstream and its feedback on the tailplane loading. The change in the time-average of the normal-force on the nacelle with respect to the prop-off case is limited. The non-negligible c_n fluctuations on the nacelle are likely the result of the separated and unsteady flow originating from the root sections of the propeller, as observed in Fig. 8. This should be considered as an artefact of the selected propeller geometry, and is not a general characteristic of the tailplane-mounted propeller configuration.

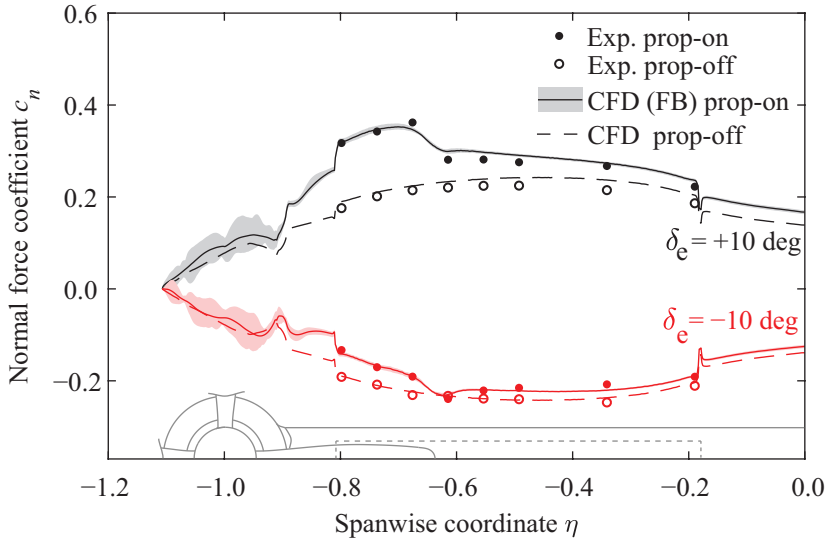

Fig. 11 Spanwise distribution of normal-force coefficient for positive and negative elevator deflection.

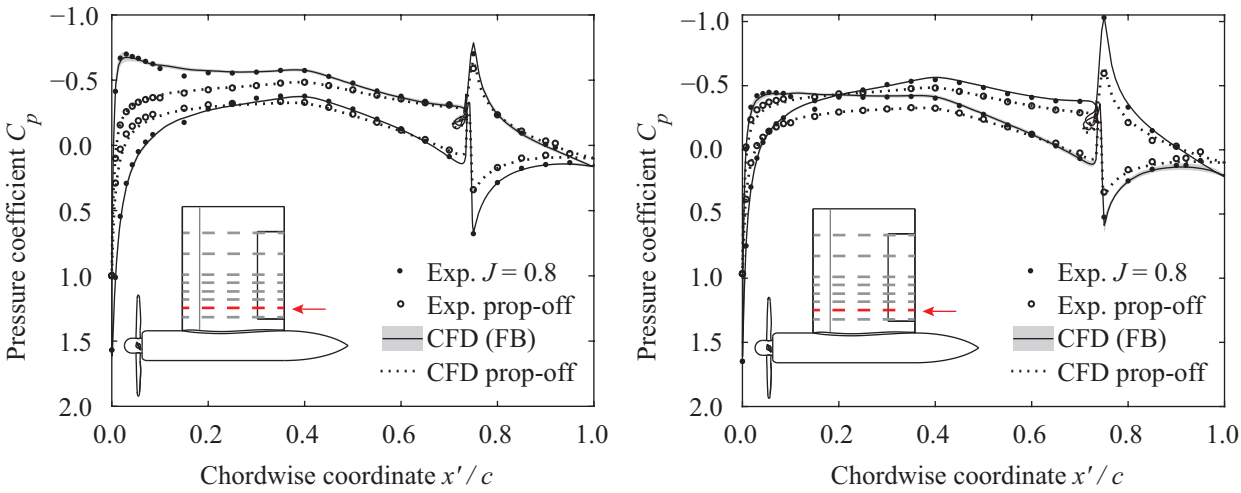

(a) $\delta_e = +10$ deg (b) $\delta_e = -10$ deg

Fig. 12 Pressure distributions inside the propeller slipstream at $\eta = -0.74$ compared to propeller-off conditions at $\alpha = 0$ deg and $\delta_e = \pm 10$ deg.

To assess the local changes to the tailplane loading caused by the interaction with the slipstream, the pressure distributions were analyzed. Figure 12 displays the measured and computed pressure distributions at a spanwise station located inside the propeller slipstream, for both the positive and negative elevator settings. It can be seen that the time-average CFD pressure distribution is very close to the experimental result, with and without the propeller. The largest deviation from the experiment occurs around $x'/c = 0.12$, which corresponds to the location of the transition strip (Fig. 3), which was not modeled in the CFD simulations. The results once more confirm that the CFD simulations are sufficiently accurate to quantify the time-averaged interaction phenomena.

The interaction with the propeller slipstream introduces a number of differences in the pressure distribution on the tailplane compared to the propeller-off case. First, for the case with the propeller present the pressure coefficient at the stagnation point is above unity due to the increased total pressure in the slipstream. This effect can also be observed on the pressure side of the elevator. Second, the increased suction occurs primarily in the leading edge region for both elevator deflections. For the case with $\delta_e = +10$ deg (Fig. 12 (a)), this is reflected in a clear increase in the suction peak, while for the case with $\delta_e = -10$ deg the suction and pressure sides are interchanged compared to the propeller-off condition. For both cases, this is due to a local increase in the angle of attack experienced by the tailplane. The effect is especially pronounced in the leading edge region of the tailplane due to the nonuniform inflow-angle profile in the propeller slipstream and local upwash due to the nacelle.

The increased suction near the leading edge is accompanied with only a moderate pressure increase on the pressure side, implying that the lift vector is tilted into the freestream direction. This tilting of the lift vector corresponds to swirl recovery by the tailplane, reducing its drag. This effect can directly be observed by comparing the drag distribution along the span of the tailplane for the propeller-off and propeller-on configurations, as plotted in Fig. 13a. For both elevator settings, the installation of the propeller increases the sectional drag coefficient with respect to the result obtained for the propeller-off configuration. This is the result of the larger dynamic pressure inside the slipstream and the modified normal-force distribution along the span. However, the case with δ_e clearly features the highest drag coefficient, confirming the expected stronger swirl recovery for the case with δ_e. The effect of lower induced losses for the $\delta_e = +10$ deg case can also be observed by comparing the $\frac{c_n}{c_d}$ ratio along the span, shown in Fig. 13b. It can be seen that the propeller installation changes the $\frac{c_n}{c_d}$ ratio over the complete tailplane. The $\frac{c_n}{c_d}$ ratio is enhanced for the case with the propeller rotating opposite to the tailplane tip-vortex. This is a direct result of the associated reduction of the swirl angle in the wake of the model, as discussed in relation to Figs. 6 and 7. It is noted that part of the differences in the spanwise distribution of $\frac{c_n}{c_d}$ may be attributed to the fact that the airfoils operate at different c_n values in the three cases, and hence at different two-dimensional $\frac{c_l}{c_d}$ ratios.

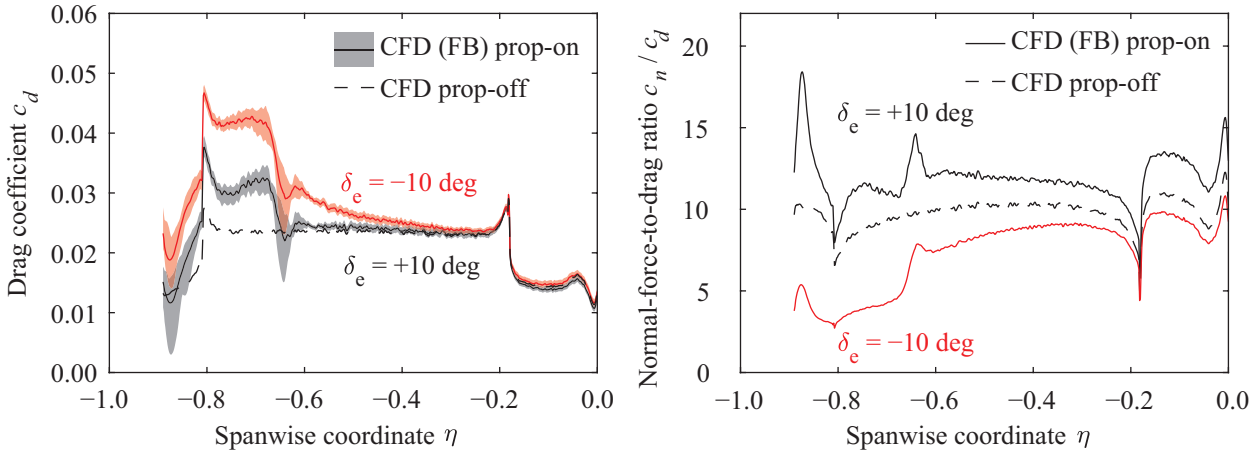

(a) Drag coefficient

(b) Normal-force-to-drag ratio

Fig. 13 Computed spanwise distributions of drag and normal-force-to-drag ratio at $\alpha = 0$ deg.

Whereas the normal-force distribution shows relatively small variations in time (Fig. 11), the fluctuations of the drag coefficient are significant along the spanwise part of the tailplane immersed in the slipstream, with the largest variations occurring near the edge of the slipstream (Fig. 13a). Therefore, it is concluded that these variations of the drag coefficient are caused by the unsteady effects associated with the periodic impingement of the propeller blade wakes and tip vortices. In Refs. [14, 21, 22] it is concluded that the largest pressure fluctuations on a lifting surface behind a propeller occur in the propeller tip-vortex region. Therefore, this spanwise location is analyzed in more detail here. Figure 14 shows measured and computed pressure distributions on the tailplane at two spanwise locations around the edge of the propeller slipstream. At a spanwise location of $\eta = -0.61$, the pressure fluctuations on the tailplane are primarily present on the advancing side (in this case the pressure side), as depicted in Fig. 14a. However, at a spanwise location of $\eta = -0.68$ (Fig. 14b), the largest fluctuations are on the retreating side of the main element. In addition to the time-averaged result with fluctuations superimposed, also a time-accurate pressure distribution is included in Fig. 14b. In this time-accurate pressure distribution, the passages of the propeller blade tip vortices over the tailplane can be recognized as the waves of increased negative pressure on the suction side of the tailplane. Going downstream, these fluctuations become less pronounced, confirming previous results [14, 21].

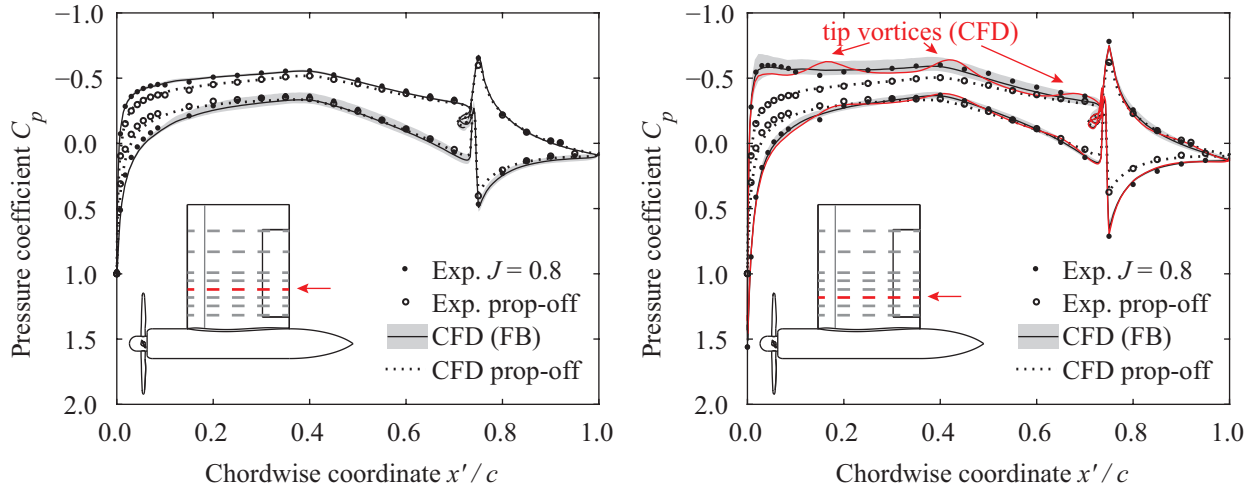

(a) $\eta = -0.61$

(b) $\eta = -0.68$

Fig. 14 Pressure distributions at two spanwise locations for the case $\alpha = 0$ deg and $\delta_e = +10$ deg.

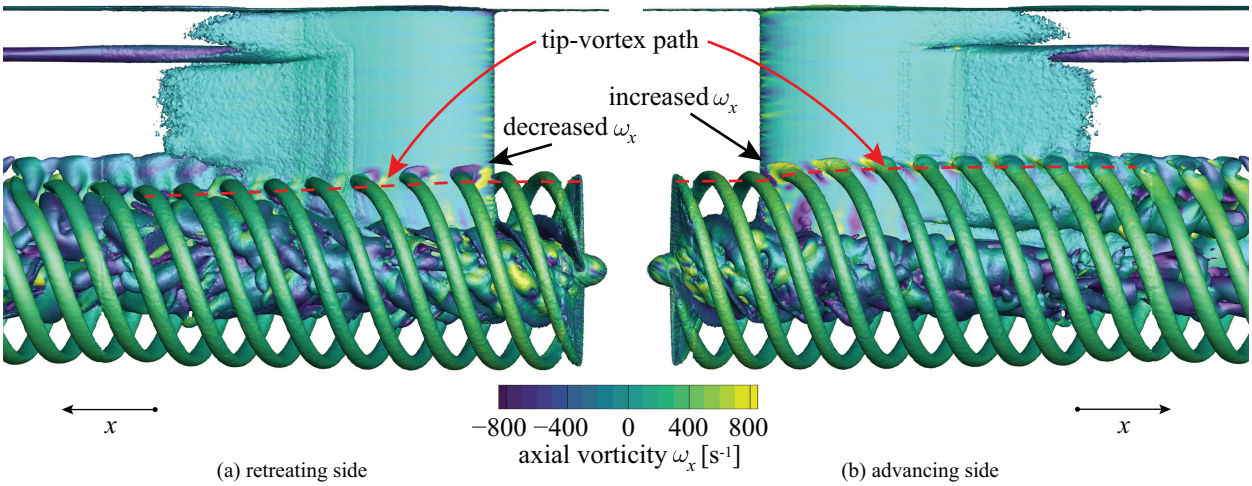

Fig. 15 Isosurface of vorticity magnitude at 800 s^{-1} for the case α = 0 deg and δ_e = +10 deg.

The observation that the pressure fluctuations are highly dependent on the chordwise and spanwise location indicates that the propeller tip vortices do not pass over the tailplane in a path parallel to the chord. To understand the displacement of the propeller slipstream caused by the interaction with the tailplane, the computed propeller vortex field was analyzed, as shown in Fig. 15. It can be seen that the propeller tip vortices which are convecting downstream in the inboard region of the tailplane follow a path not parallel to the tailplane chord. Moreover, a distinct change can be observed in the amplitude of the axial vorticity in the region where the tip-vortex impinges on the leading edge of the tailplane. On the advancing, side almost all the vorticity in the tip-vortex is oriented in the axial direction. The same holds for the retreating side, apart from the sign of ω_x, which is negative. When approaching the tailplane, the tip-vortex starts bending around the leading edge [14] and vorticity is being redistributed due to the thickness of the tailpane. This combination results in an initial displacement of the propeller slipstream near the leading edge. The remainder of the slipstream deformation is the result of the variation of circulation in the spanwise direction of the tailplane, as discussed before.

The analysis in Section IV.B showed significant variations in the propeller loading in azimuthal direction for the $\alpha = +10$ deg case. The nonuniform loading on the propeller results in a nonuniform slipstream as well, which will affect the tailplane loading distribution. Since in a realistic flight scenario the tailplane will be exposed to a range of angles of attack, the impact of nonzero angle of attack on the tailplane loading is relevant. Figure 16 displays the spanwise load distribution obtained for the case at an angle of attack of +10 deg and elevator deflection of $\delta_e = -10$ deg. Both the propeller-on and propeller-off cases are considered. The installation of the propeller results in a significant increase in normal-force along the span when compared to the propeller-off case. The fluctuations of the normal-force coefficient caused by the slipstream impingement are more pronounced than for the case of zero angle of attack (Fig. 11). This is likely due to the increased variations in propeller loading occurring for the case at nonzero angle of attack, as observed from Figs. 8 and 9. Moreover, the strength of the tip-vortex also varies in the azimuthal direction due to the azimuthally varying propeller thrust.

Apart from the increase in wing loading, Fig. 16 also displays a clear increase in normal-force on the nacelle due to the installation of the propeller, a phenomenon absent for the case at $\alpha = 0$ deg. This increase is found to be the result of two phenomena. First, the increase in propeller thrust in the wedge $\theta = 270 \pm 45$ deg (Fig. 9b) results in a significant increase in dynamic pressure on the pressure side of the nacelle. Second, it was found that the hub vortices from the propeller roll up into a system of vortices on this side of the nacelle, inducing a low pressure on the nacelle. This effect is specific to tip-mounted propellers, while the increased dynamic pressure on the pressure side of the nacelle induced by the propeller also occurs for wing-mounted propellers. Inspection of the associated pressure distributions, depicted in Fig. 17a, shows that for the case at 10 deg angle of attack, the installation of the propeller mostly affects the local pressure on the main element of the tailplane. At the elevator, on the other hand, the change in pressure distribution is smaller, especially compared to the result obtained for the case with zero angle of attack (Fig. 12b). At the edge of the slipstream (Fig. 17b), moderate pressure fluctuations occur on the retreating side of the tailplane, similar to the case without angle of attack.

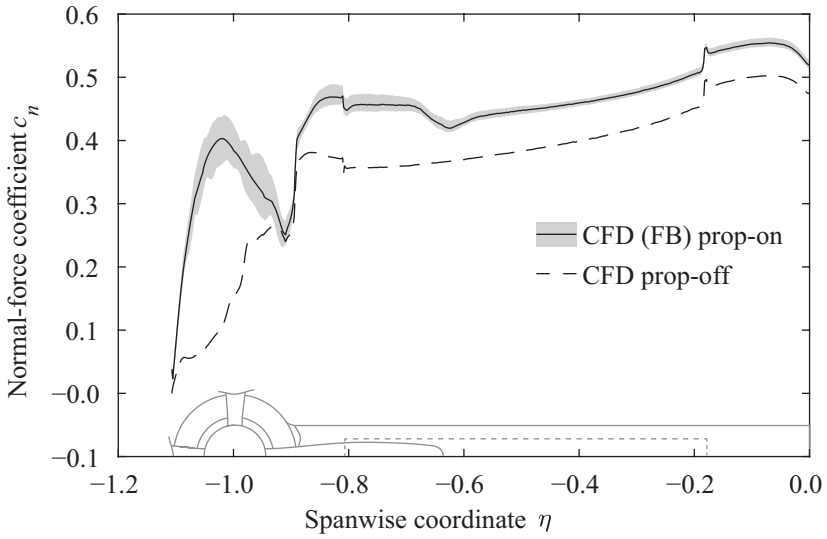

Fig. 16 Computed spanwise distributions of normal-force coefficient on the tailplane at α = +10 deg and δ_e = −10 deg.

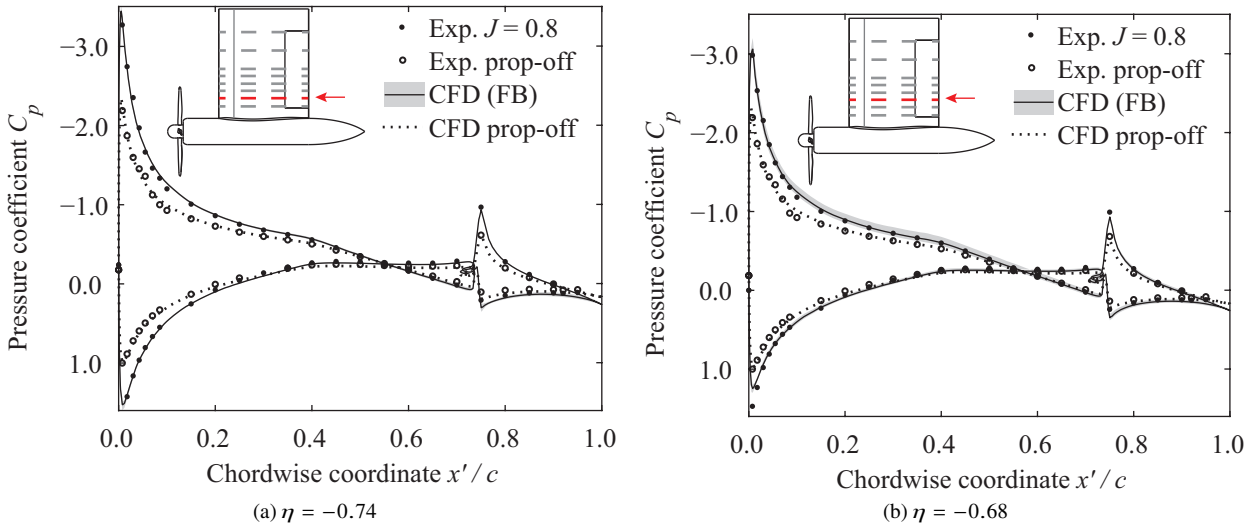

Fig. 17 Pressure distributions at two spanwise locations for the cases α = +10 deg and δ_e = −10 deg.

D. Integral Forces on the Propeller–Tailplane Model

Whereas the sectional loading distributions discussed in the previous section provide a detailed understanding of the interaction phenomena, the integral forces need to be considered to assess the overall performance of the tailplane. Therefore, this section evaluates the effects of propeller installation on the total forces acting on the propeller–tailplane model. The experimental data are used, as measured with the external balance (Section II.B). Figure 18 displays the development with propeller thrust setting of four of the aerodynamic quantities relevant for a propeller–tailplane combination: the normal-force, the normal-force gradient, the change in normal-force due to elevator deflection, and the maximum and minimum normal-force. The measured results include the forces generated by the propeller, since the propeller loading was not measured separately from the tailplane loading.

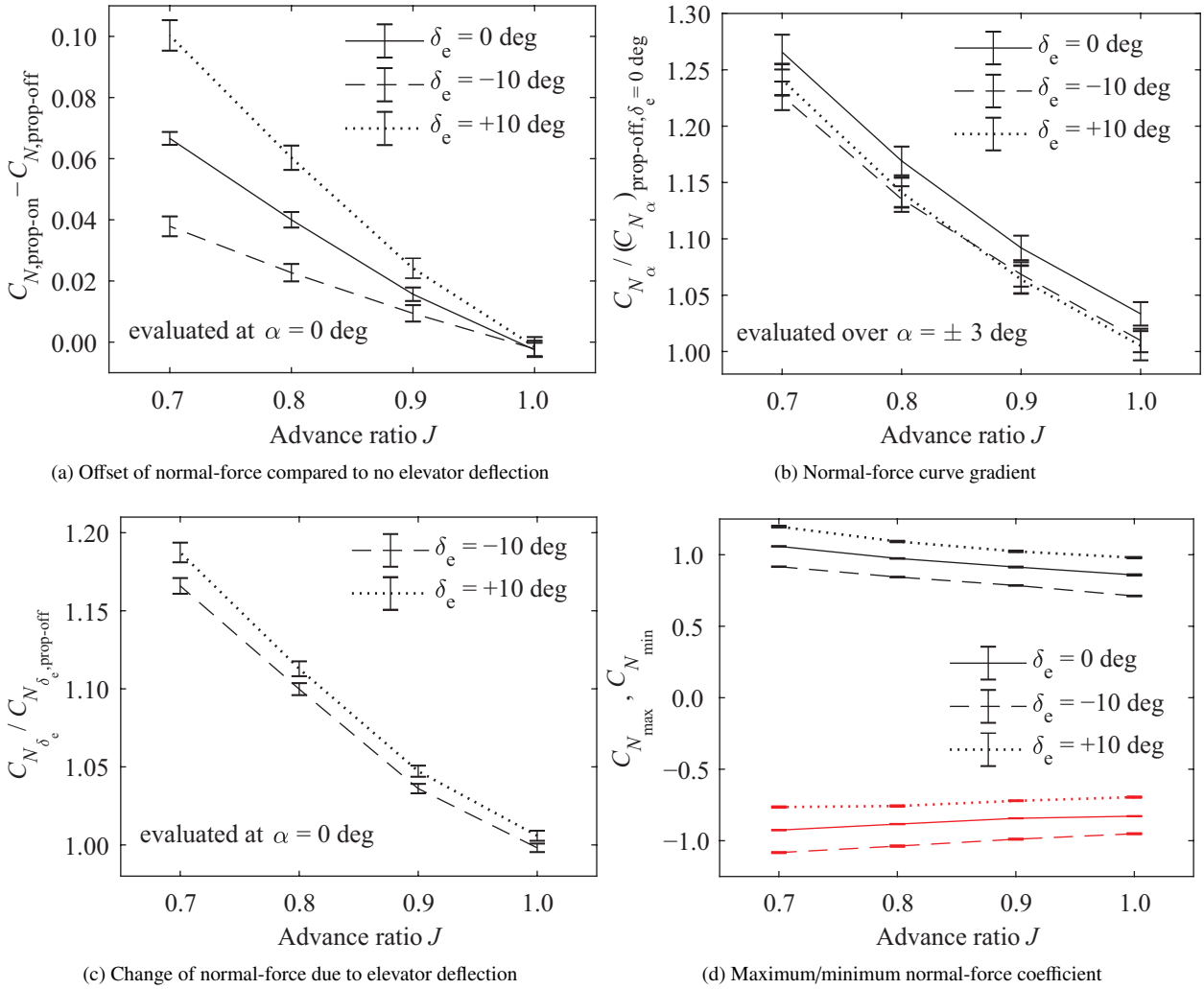

(a) Offset of normal-force compared to no elevator deflection

(b) Normal-force curve gradient

(c) Change of normal-force due to elevator deflection

(d) Maximum/minimum normal-force coefficient

Fig. 18 Measured effect of propeller installation on the integral forces generated by the propeller–tailplane model. The error bars are computed by propagating the variations of the balance measurements.

The spanwise loading distributions discussed in Section IV.C showed that a positive elevator deflection results in significantly higher loading at $\alpha = 0$ deg than a negative elevator deflection. This is confirmed by Fig. 18a. Regardless of the elevator setting in propeller-off condition, the propeller-induced swirl causes an increase in normal-force with increasing thrust setting. However, the extend in which C_N is changed by the propeller depends on the direction in which the elevator is deflected. This implies that for the same normal-force on the tailplane, a different elevator deflection needs to be selected depending on the propeller rotation direction.

Figure 18b shows the gradient of the normal-force curve with angle of attack, C_{N_α}, relative to the propeller-off case for the four analyzed advance ratios. As expected, C_{N_α} increases with increasing thrust setting for all flap settings. For the case with zero flap deflection, the normal-force gradient was enhanced by around 28% at the highest thrust setting considered ($J = 0.7$). With the elevator deflected, the normal-force gradient decreased due to the flap-edge vortices which reduce the effective aspect ratio of the tailplane. The propeller is shown to increase the normal-force gradient more for the positive elevator deflection than for the negative elevator deflection. This is directly related to the lower induced losses occurring for the case with positive elevator deflection, as discussed before in Sections IV.A and IV.C.

The effectiveness of the elevator in changing the normal-force on the tailplane is evaluated in Fig. 18c, again relative to the results obtained for the propeller-off case. For both elevator settings, the effectiveness of the elevator increases with increasing propeller thrust setting. The fraction of the elevator which is inside the propeller slipstream experiences a higher dynamic pressure than freestream conditions, enhancing its effectiveness. The best performance is obtained for

the positive elevator deflection. It is expected that this is a consequence of the difference in normal-force curve slope of the tailplane for the two elevator settings (Fig. 18b).

As the lift coefficient varies significantly over the span due to the propeller swirl, it can be expected that the stall behavior is a function of the thrust setting of the propeller. Figure 18d shows an increase in magnitude of both the maximum and minimum normal-force coefficient with increasing propeller thrust. An important contributor to this change is the increased dynamic pressure on the tailplane region washed by the propeller slipstream. For a given propeller advance ratio, the maximum normal-force depends on the elevator deflection. For example, for $\alpha > 0$ deg, a negative elevator deflection results in a stronger adverse pressure gradient on the suction side than a positive elevator deflection, hence the boundary layer is more prone to separation at the negative elevator setting. The stall of the tailplane model is characterized by leading edge stall at the inboard sections. In the propeller-off condition, at around $\alpha = 18$ deg the spanwise region $-0.5 < \eta \leq 0.0$ experiences a completely separated flow on the suction side. However, the outboard sections still exhibit attached flow in the leading edge region, although the separation point has moved upstream compared to lower angles of attack. This implies that the outboard sections have not reached their maximum lift coefficient at the tailplane stall angle of attack. When the propeller is installed, the lift on these sections is increased, which leads to an increase in the integral tailplane loading. Additionally, the normal-force induced by the propeller on the nacelle as mentioned in Section IV.C also enhances the loading on the outboard sections. It is expected that this phenomenon contributes to the maximum normal-force of the tailplane. Although there is a local increase in angle of attack due to the swirl of the slipstream, for a given elevator deflection the angle of attack at which the maximum normal-force coefficient was obtained, was approximately the same for the considered advance ratios. It is noted that at very high thrust settings the tailplane stall may be initiated in the outboard regions due to the associated large swirl angles. However, these conditions are not considered for the current paper.

E. Tailplane Loading for a Co-Rotating Propeller Configuration

The previous results have shown a significant difference in loading distribution on the tailplane depending on the direction in which the elevator is deflected. Due to the presence of the ground plane, the experiments and CFD analysis resemble two counter-rotating propellers mounted on each tip of a horizontal tailplane. However, as mentioned in the introduction, a co-rotating configuration is likely to be preferred for an industrial application. In that case there is an inboard-up (IU) and an outboard-up (OU) rotating propeller, creating an asymmetric tailplane loading. Such an asymmetry in loading requires trim to avoid a rolling and yawing moment. To quantify the differences between the co-rotating and counter-rotating cases for the current geometry, the full span of the tailplane was simulated with both elevators deflected by +10 deg for the co-rotating case, as depicted in Fig. 19. The counter-rotating cases were simulated with the same boundary conditions as presented in Section III. Because the no-slip wall boundary condition was present for the counter-rotating cases and absent in the co-rotating simulations, the loading distributions cannot be compared around the tailplane symmetry plane. The input for the actuator-disk was an extracted blade loading from both the $\delta_e = +10$ deg and $\delta_e = -10$ deg full-blade propeller simulations. This approach assumes that the nonuniform propeller loading for the co-rotating case was the same as for the counter-rotating case.

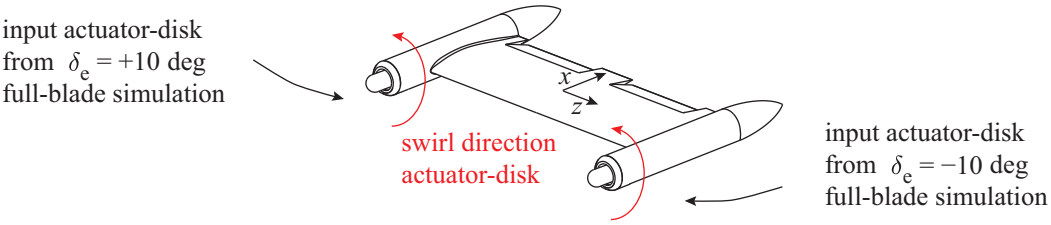

Fig. 19 Schematic of the analyzed co-rotating case by means of actuator-disks.

Figure 20a presents the resulting spanwise distributions of the normal-force coefficient for the co-rotating and counter-rotating cases. For the counter-rotating case, both the inboard-up and outboard-up results are included. The propeller-off result is also shown for reference. Toward the tailplane tip, the normal-force distribution is comparable to the co-rotating and counter-rotating cases. Toward the spanwise location $\eta = 0$, the co-rotating case displays an increasing deviation from the counter-rotating cases, with a reduced normal-force on the inboard-up side and an increased normal-force on the outboard-up side compared to the counter-rotating cases. This the result of the differences between the trailing vortex systems for both cases. A relatively large normal-force gradient can be observed at $\eta = 0$ for

the counter-rotating cases and propeller-off case, which is expected to be the result of the modeling of the ground-plane as a no-slip wall. Compared to propeller-off conditions, the co-rotating case has a net increase in the total normal-force on the tailplane, due to the higher c_n on the inboard up side. This means that for a negative elevator deflection, the propeller installation results in a more negative normal-force compared to propeller-off conditions. Figure 20b presents the distribution of normal-force-to-drag ratio along the tailplane span. The same trends can be observed compared to the distribution of normal-force. It can be seen that toward the tailplane tip, the normal-force-to-drag ratio of the inboard-up co-rotating case is comparable with the inboard-up counter-rotating case. The same holds for the outboard-up side of the tailplane. Toward the spanwise location $\eta = 0$, the co-rotating case displays an increasing deviation from the counter-rotating cases, with a reduced normal-force-to-drag ratio on the inboard-up side and an increased normal-force-to-drag on the outboard-up side compared to the associated counter-rotating cases. This is a direct result of the induced effect of the vortex system on the two tailplane sides which influences the local normal-force-to-drag ratio. From the distributions it becomes clear that the integral normal-force-to-drag ratio of the tailplane is only slightly changed compared to propeller-off condition. Therefore, the potential benefit in terms of the tailplane normal-force-to-drag by using tip-mounted propellers is limited if the propellers are co-rotating.

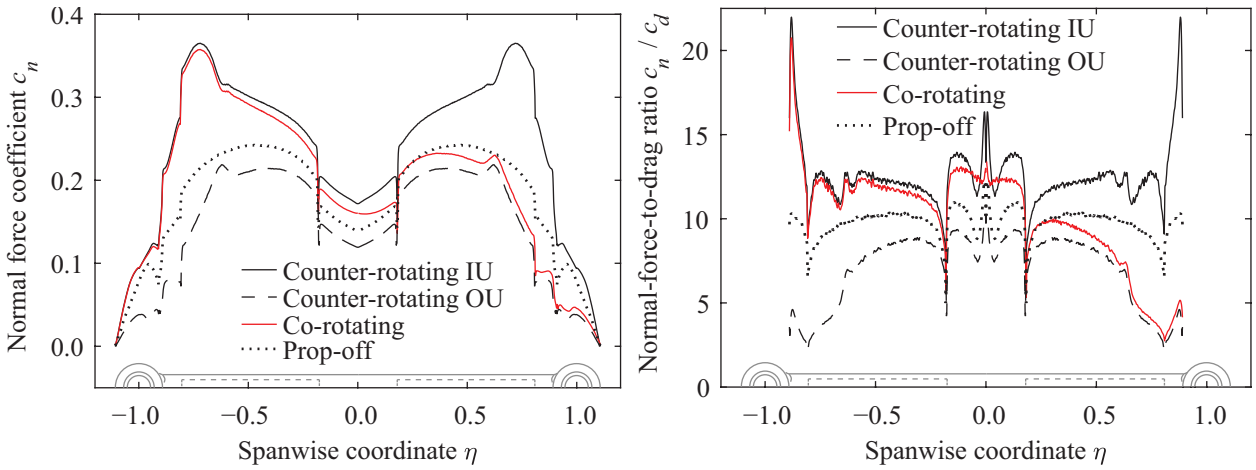

(a) Distribution of normal-force coefficient.

(b) Distribution of normal-force-to-drag ratio.

Fig. 20 Computed spanwise load distribution on the tailplane for co-rotating and two counter-rotating propeller installations at $J = 0.8$ and $\alpha = 0$ deg. The propellers are modeled by actuator disks.

V. Conclusions

This paper has presented a study of the aerodynamic interaction effects for a tip-mounted propeller installed on a horizontal tailplane. Based on measurements of the swirl angle downstream of the tailplane and propeller, it was concluded that a significant reduction in the mean swirl angle occurs if the elevator is deflected such that the tailplane tip-vortex is in opposite direction of the propeller swirl.

Based on a numerical assessment of the upstream effect of the tailplane on the propeller, the following conclusions were drawn:

- The propeller installation results in a 3% increase of the time-averaged thrust compared to isolated conditions, both at $\alpha = 0\,\text{deg}$ and $\alpha = +10\,\text{deg}$. Both positive and negative elevator deflections result in a propeller normal-force of approximately 2% of the installed thrust.
- At zero angle of attack, the variation in thrust on the individual blades over one revolution were found to be in the order of ±5% of the time-averaged value. Variations in the thrust of the four blades combined were found to be negligible.

Analysis of the measured and computed results led to the following conclusions related to the tailplane loading:

- The rotation direction of the tailplane tip-vortex relative to the propeller swirl significantly affects the loading distribution on the tailplane. An elevator deflection resulting in a tailplane tip-vortex which is contra-rotating with the propeller swirl, results in increased loading on the tailplane and an increase of the tailplane's normal-force gradient. In that case, there is an increased normal-force-to-drag ratio along the complete span of the tailplane compared to propeller-off conditions. The opposite is the case for a tailplane tip-vortex which is co-rotating with the propeller swirl.
- Changes to the time-averaged pressure distribution inside the propeller slipstream compared to propeller-off conditions occur primarily in the leading edge region of the tailplane. Time-dependent changes to the pressure distribution are confirmed to occur primarily in the region where the propeller tip vortices pass over the tailplane. The associated variations in the sectional normal-force coefficient are in the order of $c_n' = \pm 0.01$ at intermediate propeller loading conditions.
- At an angle of attack of 10 deg, a significant normal-force is generated by the nacelle. It is found that this is the combined result of the nonuniform loading on the propeller resulting in a high dynamic pressure on the pressure side of the nacelle and the roll up of propeller hub vortices inducing a low pressure on the suction side of the nacelle.
- The elevator effectiveness depends on the propeller thrust setting and the direction of the elevator deflection. For an inboard-up rotating propeller, a positive elevator deflection is more effective than a negative deflection.
- At the considered propeller operating conditions, the maximum normal-force of the propeller–tailplane configuration increases with increasing thrust coefficient.
- Potential benefits of a higher normal-force-to-drag ratio of the tailplane compared to propeller-off conditions by tip-mounted propeller installation are limited for a co-rotating propeller configuration.

Acknowledgments

The authors would like to thank Stefan Bernardy and Leo Molenwijk for their technical assistance during the experimental campaign. Furthermore, the help of Daniele Ragni during the setup of the PIV measurements is much appreciated.

References

[1] Whitlow, J. B., and Sievers, G. K., "Fuel Savings Potential of the NASA Advanced Turboprop Program," Tech. Rep. TM-83736, NASA, 1984.

[2] Goldsmith, I. M., "A Study to Define the Research and Technology Requirements for Advanced Turbo/Propfan Transport Aircraft," Tech. Rep. CR-166138, NASA, 1981.

[3] Sullivan, W. E., Turnberg, J. E., and Violette, J. A., "Large-Scale Advanced Prop-Fan Blade Design," Tech. Rep. CR-174790, NASA, 1984.

[4] Patterson, M. D., Derlaga, J. M., and Borer, N. K., "High-Lift Propeller System Configuration Selection for NASA's SCEPTOR Distributed Electric Propulsion Flight Demonstrator," *16th AIAA Aviation Technology, Integration, and Operations Conference*, 2016. doi:10.2514/6.2016-3922.

[5] Kennedy, J., Eret, P., and Bennett, G., "A parametric study of installed counter rotating open rotors," *19th AIAA/CEAS Aeroacoustics Conference*, 2013. doi:10.2514/6.2013-2094.

[6] Stuermer, A., and Yin, J., "The Case for Counter-Rotation of Installed Contra-Rotating Open Rotor Propulsion Systems," *30th AIAA Applied Aerodynamics Conference*, 2012. doi:10.2514/6.2012-2785.

[7] Boctor, M.L., Clay, C.W. and Watson, C.F., "An Analysis of Prop-Fan Airframe Aerodynamic Integration," Tech. Rep. CR 152186, NASA, 1978.

[8] Applin, Z. T., and Coe, P. L., Jr, "Low-Speed Stability and Control Characteristics of a Transport Model with Aft-Fuselage-Mounted Advanced Turboprops," Tech. Rep. NT-2535, NASA, 1986.

[9] Veldhuis, L.L.M., "Propeller Wing Aerodynamic Interference," Ph.D. Thesis, Delft University of Technology, Delft, The Netherlands, 2005.

[10] Kroo, I., " Propeller/wing integration for minimum induced loss," *Journal of Aircraft*, Vol. 23, No. 7, 1986, pp. 561–565. doi:10.2514/3.45344.

[11] Miranda, L. R. and Brennan, J. E., "Aerodynamic effects of wingtip-mounted propellers and turbines," *AIAA 4th Applied Aerodynamics Conference*, 1986. doi:10.2514/6.1986-1802.

[12] Patterson, Jr, J. C., and Bartlett, G.R., "Evaluation of Installed Performance of a Wing-Tip-Mounted Pusher Turboprop on a Semispan Wing," Tech. Rep. TP-2739, NASA, 1978.

[13] Snyder, Jr, M.H. and Zumwalt, G.W., "Effects of wingtip-mounted propellers on wing lift and induced drag," *Journal of Aircraft*, Vol. 6, No. 5, 1969, pp. 392–397. doi:10.2514/3.44076.

[14] Sinnige, T., de Vries, R., Della Corte, B., Avallone, F., Ragni, D., Eitelberg, G., and Veldhuis, L. L. M., "Unsteady Pylon Loading Caused by Propeller-Slipstream Impingement for Tip-Mounted Propellers," *Journal of Aircraft (in press).*, 2017.

[15] Stokkermans, T. C. A., van Arnhem, N., Sinnige, T. and Veldhuis, L. L. M., "Validation and Comparison of RANS Propeller Modeling Methods for Tip-Mounted Applications," *AIAA Science and Technology Forum and Exposition*, 2018.

[16] ANSYS® Academic Research Release 16.0, "Help System, Fluent," ANSYS, Inc.

[17] Whitfield, L., and Jameson, A., "Euler equation simulation of propeller-wing interaction in transonic flow," *Journal of Aircraft*, Vol. 21, No. 11, 1987, pp. 835–839. doi:10.2514/3.45052.

[18] Samuelsson, I., "Low speed wind tunnel investigation of propeller slipstream aerodynamic effects on different nacelle/wing combinations," Tech. Rep. FFA TN 1990-24, Flygtekniska Försöksanstalten, 1990.

[19] de Young, J., "Propellers at high incidence," *Journal of Aircraft*, Vol. 23, No. 3, 1965, pp. 241–250. doi:10.2514/3.43646.

[20] Ortun, B., Boisard, R., and Gonzalez-Martino, I., "In-plane airloads of a propeller with inflow angle: prediction vs. experiment," *30th Applied Aerodynamics Conference*, 2012. doi:10.2514/6.2012-2778.

[21] Johnston, R. T. and Sullivan, J. P., "Unsteady wing surface pressures in the wake of a propeller," *Journal of Aircraft*, Vol. 30, No. 5, 1993, pp. 644–651. doi:10.2514/3.46393.

[22] Ljunggren, S., Samuelsson, I. and Widig, K., "Slipstream-induced pressure fluctuations on a wing panel," *Journal of Aircraft*, Vol. 26, No. 10, 1989, pp. 914–919. doi:10.2514/3.45861.

This article has been cited by:

1. Eduardo J. Alvarez, Judd Mehr, Andrew Ning. FLOWUnsteady: An Interactional Aerodynamics Solver for Multirotor Aircraft and Wind Energy . [Abstract] [PDF] [PDF Plus]
2. Nando van Arnhem, Reynard de Vries, Tomas Sinnige, Roelof Vos, Leo L. M. Veldhuis. 2022. Aerodynamic Performance and Static Stability Characteristics of Aircraft with Tail-Mounted Propellers. *Journal of Aircraft* **59**:2, 415-432. [Abstract] [Full Text] [PDF] [PDF Plus] [Supplementary Material]
3. Tomas Sinnige, Robert Nederlof, Nando van Arnhem. Aerodynamic Performance of Wingtip-Mounted Propellers in Tractor and Pusher Configuration . [Abstract] [PDF] [PDF Plus]
4. Maurice Hoogreef, Reynard de Vries, Tomas Sinnige, Roelof Vos. Synthesis of Aero-Propulsive Interaction Studies Applied to Conceptual Hybrid-Electric Aircraft Design . [Abstract] [PDF] [PDF Plus]
5. Tomas Sinnige, Tom Stokkermans, Nando van Arnhem, Leo L. Veldhuis. Aerodynamic Performance of a Wingtip-Mounted Tractor Propeller Configuration in Windmilling and Energy-Harvesting Conditions . [Citation] [PDF] [PDF Plus]
6. Nando van Arnhem, Reynard de Vries, Roelof Vos, Leo L. Veldhuis. Aerodynamic Performance of an Aircraft Equipped with Horizontal Tail Mounted Propellers . [Citation] [PDF] [PDF Plus]
7. Tomas Sinnige, Biagio Della Corte, Reynard De Vries, Francesco Avallone, Roberto Merino-Martínez, Daniele Ragni, Georg Eitelberg, Leo L. M. Veldhuis. 2019. Alleviation of Propeller-Slipstream-Induced Unsteady Pylon Loading by a Flow-Permeable Leading Edge. *Journal of Aircraft* **56**:3, 1214-1230. [Abstract] [Full Text] [PDF] [PDF Plus]
8. Tom C. A. Stokkermans, Nando van Arnhem, Tomas Sinnige, Leo L. M. Veldhuis. 2019. Validation and Comparison of RANS Propeller Modeling Methods for Tip-Mounted Applications. *AIAA Journal* **57**:2, 566-580. [Abstract] [Full Text] [PDF] [PDF Plus]
9. Nando v. Arnhem, Roelof Vos, Leo L. Veldhuis. Aerodynamic Loads on an Aft-Mounted Propeller Induced by the Wing Wake . [Citation] [PDF] [PDF Plus]
10. Tom Schouten, Maurice Hoogreef, Roelof Vos. Effect of Propeller Installation on Performance Indicators of Regional Turboprop Aircraft . [Citation] [PDF] [PDF Plus]
11. Tomas Sinnige, Nando van Arnhem, Tom C. A. Stokkermans, Georg Eitelberg, Leo L. M. Veldhuis. 2019. Wingtip-Mounted Propellers: Aerodynamic Analysis of Interaction Effects and Comparison with Conventional Layout. *Journal of Aircraft* **56**:1, 295-312. [Abstract] [Full Text] [PDF] [PDF Plus] [Supplementary Material]
12. Tom C. Stokkermans, Nando v. Arnhem, Tomas Sinnige, Leo L. Veldhuis. Validation and Comparison of RANS Propeller Modeling Methods for Tip-Mounted Applications . [Citation] [PDF] [PDF Plus]